LETTERS
https://doi.org/10.1038/s41565-020-0708-3
nature nanotechnology

Check for updates

Visualization of moiré superlattices

Leo J. McGilly[1], Alexander Kerelsky[1], Nathan R. Finney[2], Konstantin Shapovalov[3], En-Min Shih[1], Augusto Ghiotto[1], Yihang Zeng[1], Samuel L. Moore[1], Wenjing Wu[4], Yusong Bai[4], Kenji Watanabe[5], Takashi Taniguchi[5], Massimiliano Stengel[3,6], Lin Zhou[4,7], James Hone[2], Xiaoyang Zhu[4], Dmitri N. Basov[1], Cory Dean[1], Cyrus E. Dreyer[8,9] and Abhay N. Pasupathy[1]✉

Moiré superlattices in van der Waals heterostructures have given rise to a number of emergent electronic phenomena due to the interplay between atomic structure and electron correlations. Indeed, electrons in these structures have been recently found to exhibit a number of emergent properties that the individual layers themselves do not exhibit. This includes superconductivity[1,2], magnetism[3], topological edge states[4,5], exciton trapping[6] and correlated insulator phases[7]. However, the lack of a straightforward technique to characterize the local structure of moiré superlattices has thus far impeded progress in the field. In this work we describe a simple, room-temperature, ambient method to visualize real-space moiré superlattices with sub-5-nm spatial resolution in a variety of twisted van der Waals heterostructures including, but not limited to, conducting graphene, insulating boron nitride and semiconducting transition metal dichalcogenides. Our method uses piezoresponse force microscopy, an atomic force microscope modality that locally measures electromechanical surface deformation. We find that all moiré superlattices, regardless of whether the constituent layers have inversion symmetry, exhibit a mechanical response to out-of-plane electric fields. This response is closely tied to flexoelectricity wherein electric polarization and electromechanical response is induced through strain gradients present within moiré superlattices. Therefore, moiré superlattices of two-dimensional materials manifest themselves as an interlinked network of polarized domain walls in a non-polar background matrix.

Existing methods to visualize moiré superlattices with high resolution, including transmission electron microscopy[8,9] and scanning tunnelling microscopy[10,11] require some combination of ultra-high vacuum, low temperature, complex setups or specialized sample preparation that makes these methods impractical to apply on a usual basis to characterize moiré structures. Other methods such as near-field optics[5] and transport with multiple contacts[1–3,7] are limited in resolution to length scales above the moiré periods of interest, which are typically in the 10-nm size scale. There is, thus, an urgent need for a facile method to characterize moiré superlattices in these samples. As an example, consider twisted bilayer graphene (tBLG); a stack of two monolayers of graphene with different lattice orientations, as can be seen in Fig. 1a–c. When the two lattices are in orientational registry, there are still a number of ways in which the two layers can be arranged corresponding to different translations of the lattices. The most energetically costly configuration is 'AA' stacking (Fig. 1a). 'Bernal' or 'AB' stacking (Fig. 1b) is the energetically preferred arrangement while at the interface of two Bernal regions is 'saddle point' stacking, as seen in Fig. 1c. The rotational misalignment of layers enforces the creation of a moiré superlattice that necessarily contains each of the stacking domains in proportions that are related to the twist angle. Below a critical angle[12] there is an energetic drive to form a moiré pattern that maximizes the energetically favourable AB stacking at the expense of AA sites through lattice reconstruction that leads to the creation of discrete stacking domains and domain walls[8,9]. Being able to visualize the details of rotation angle, stacking domains and domain walls in a simple way would open up these structures to reproducible experimentation.

We begin by discussing experiments on low-twist angle tBLG before generalizing our results to a wide range of materials. Fig. 1e shows a schematic of the piezoresponse force microscopy (PFM) technique, which provides information about the local electromechanical response (see Methods). As shown in Fig. 1g,h, PFM produces amplitude and phase images that show the domain wall array of the tBLG moiré pattern. Simple inspection of the amplitude shows that a large response is found at the domain wall regions and at the AA stacking sites, while a smaller but non-zero response is found in the AB domains. This is an interesting but surprising result as from a simple symmetry perspective there is no reason to believe that bilayer graphene, which is centrosymmetric, would be electromechanically active through the piezoelectric effect that is usually probed by PFM (a number of studies suggest graphene can be piezoelectric given certain conditions but these are not applicable here[13–17]). It should be noted that the height image (Supplementary Fig. 1) does not show any substantial topography, ruling out crosstalk from large surface features. However, PFM can give responses that seem to indicate piezoelectric or even ferroelectric behaviour but which on closer inspection turn out to be electrostatic[18], electrochemical effects[19] or even cantilever dynamics[20]. Therefore, careful analysis is required.

Regardless of the origin of the contrast obtained here, the technique is beneficial for fast and simple identification of moiré domain patterns in twisted bilayer systems. We applied this technique to a number of materials systems for which examples are given in Fig. 2. PFM proved capable of revealing the moiré patterns in multiple systems with astounding resolution down to moiré wavelengths below 5 nm (Fig. 2j–l) and over several micrometre-length scales

[1]Department of Physics, Columbia University, New York, NY, USA. [2]Department of Mechanical Engineering, Columbia University, New York, NY, USA. [3]Institute of Materials Science of Barcelona, Bellaterra, Spain. [4]Department of Chemistry, Columbia University, New York, NY, USA. [5]National Institute for Materials Science, Tsukuba, Japan. [6]ICREA–Instució Catalana de Recerca i Estudis Avançats, Barcelona, Spain. [7]College of Engineering and Applied Sciences, Nanjing University, Nanjing, China. [8]Department of Physics and Astronomy, Stony Brook University, Stony Brook, NY, USA. [9]Center for Computational Quantum Physics, Flatiron Institute, New York, NY, USA. ✉e-mail: apn2108@columbia.edu

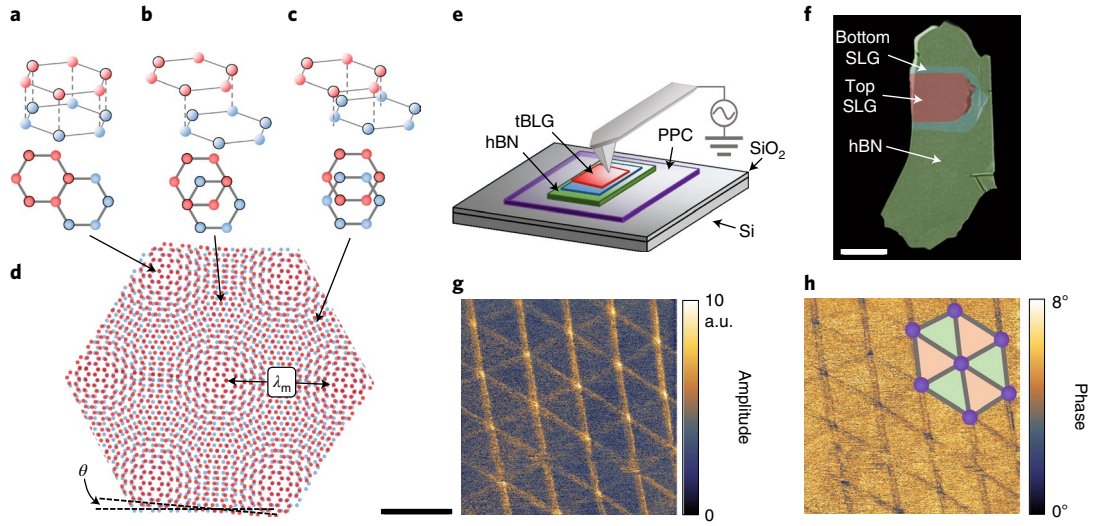

Fig. 1 | Stacking order domains in twisted bilayer graphene and visualization by PFM. a–d, The three main bilayer graphene stacking configurations are shown (AA (**a**), AB (**b**) and SP stacking (**c**)) and their locations within a moiré pattern with a twist of angle θ and a wavelength of λ_m (**d**). **e**,**f**, The PFM experiment and the sample geometry of a typical setup (**e**) and an optical microscopy image (**f**) with colour-coded areas showing the vdW heterostructure. **g**,**h**, The moiré pattern superlattice is revealed through 'lateral-mode' PFM amplitude (**g**) and phase (**h**) images. The overlay shows the stacking domains; AA sites in purple, AB/BA domains in green and orange and domain walls in grey. SP, saddle point. Scale bars, 500 nm (**g**) and 10 μm (**f**).

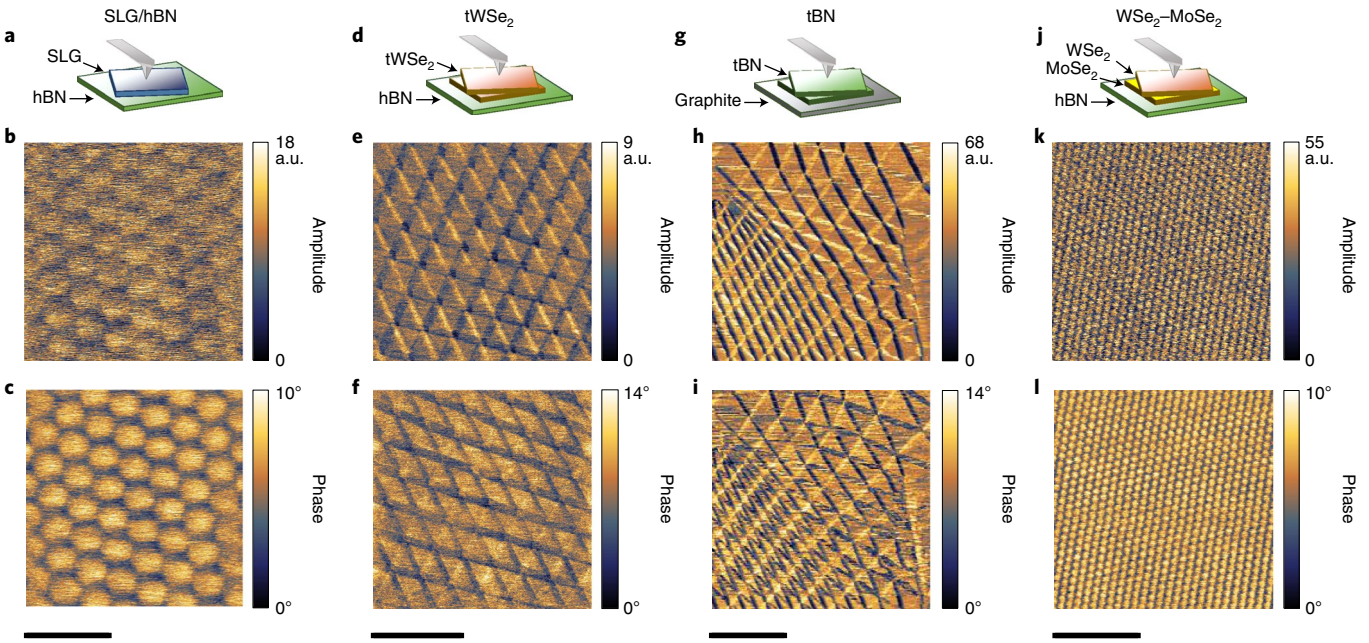

Fig. 2 | Examples of PFM imaging of moiré superlattices in various vdW heterostructures. a–l, Schematic representations (top row), corresponding PFM amplitude (middle row) and phase (bottom row) of monolayer graphene on BN (**a**–**c**), twisted bilayer WSe_2 (**d**–**f**), twisted bilayer BN (**g**–**i**) and twisted WSe_2–$MoSe_2$ heterobilayer (**j**–**l**). The lateral PFM mode is used for **d**–**i** and the vertical mode for **a**–**c** and **j**–**l**. Scale bars, 30 nm (**c**), 200 nm (**f**), 500 nm (**i**) and 50 nm (**l**).

(Extended Data Fig. 1) limited only by sample size. This imaging technique is not limited to semimetallic graphene but is also clearly observed in semiconductors such as WSe_2 (Fig. 2d–f) and $MoSe_2$, and insulators such as boron nitride (BN) (Fig. 2g–i) and their heterostructures (Fig. 2a–c). Additionally, the technique is able to simultaneously image multiple moiré superlattices (Extended Data Fig. 2). In fact, we believe that this technique will be able to accurately map the moiré pattern of any two-dimensional materials system. The universal applicability indicates that the underlying origin of this phenomenon is equally universal and does not depend on the detailed behaviour of the constituent two-dimensional materials.

To illuminate the nature of the electromechanically induced surface deformation we first perform a type of simple 'vector' PFM[21] for our prototypical system of tBLG as is outlined in Fig. 3. PFM is sensitive to out-of-plane (vertical) and in-plane (lateral) surface displacements that can be independently detected by the

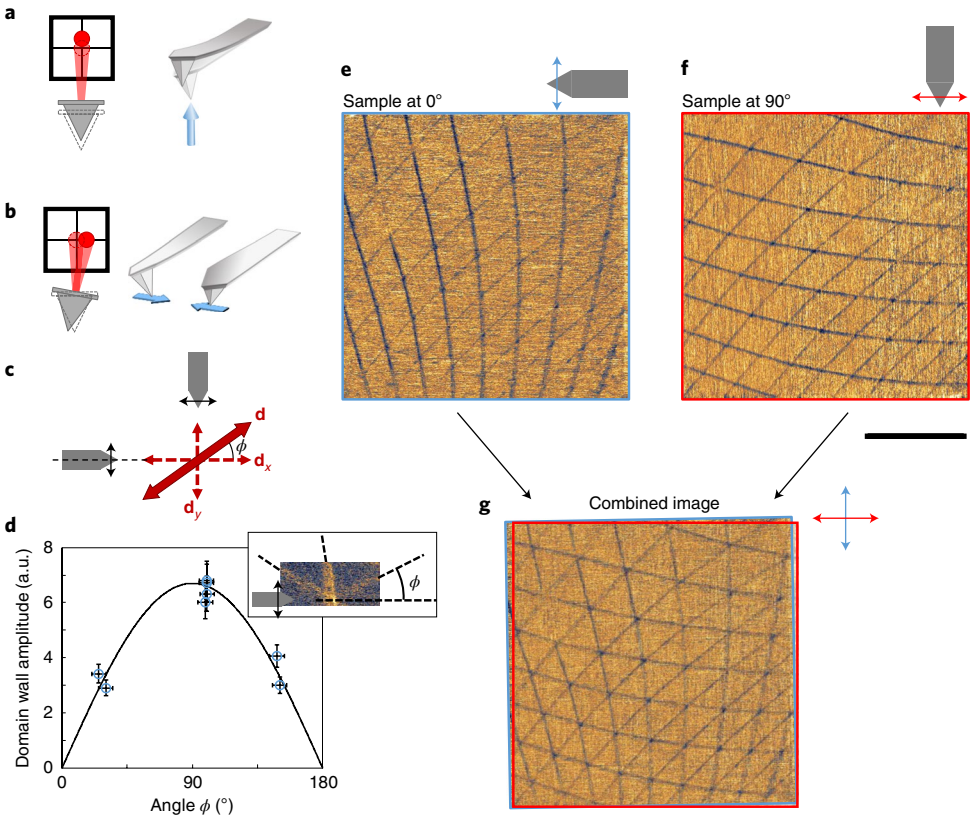

Fig. 3 | PFM imaging modes, cantilever dynamics and the resulting effects on contrast in tBLG. a, A vertical displacement of the cantilever due to an out-of-plane surface deformation (blue arrow) leads to a vertical deflection on the photodiode detector. **b**, In-plane surface deformation (blue arrows) leads to torsional bending of the cantilever and a resulting lateral deflection on the photodiode detector. **c**, For an in-plane surface deformation vector **d**, detection for lateral PFM will only measure the component that is oriented perpendicular to the cantilever axis denoted as $\mathbf{d}_x$ (cantilever, grey pointed rectangle; axis, black dotted line; measurement sensitivity direction, black double-headed arrow) as seen. To measure the orthogonal component, $\mathbf{d}_y$, physical rotation of the sample is required so that reconstruction of the total in-plane surface displacement **d**, is possible through 'vector' PFM. **d**, A measure of the apparent domain wall amplitude as a function of the angle separation between the cantilever axis and the domain wall (inset) shows results (blue circles) consistent with a sine function (solid black line). Error bars in **d** incorporate the natural variation in angle and amplitude of the walls. **e**–**g**, Simple vector PFM (lateral mode) performed by a sample rotation of ~90°; phase images at 0° (**e**) and 90° (**f**) can be recombined to reconstruct the full moiré pattern (**g**). Scale bar in **f**, 1 µm.

quadrant photodiode detector as is illustrated in Fig. 3a,b. For lateral displacements perpendicular to the cantilever axis, the cantilever deforms through torsion resulting in a lateral signal on the photodiode. In contrast, lateral surface displacement parallel to the axis results in cantilever flexure, which is measured as a vertical deflection on the photodiode detector (Supplementary Fig. 2) and is more difficult to distinguish from a real vertical surface displacement. For bilayer graphene, we determined PFM contrast consistent with an in-plane displacement component aligned with the cantilever axis and measured through flexure (Supplementary Fig. 3). This is direct evidence that PFM measures a largely in-plane response and any apparent vertical signal is dominated by the in-plane flexural crosstalk.

Figure 3d shows the in-plane PFM amplitude measured across domain walls as a function of the domain wall angle relative to the cantilever axis. The measured lateral signal is a minimum/zero when the domain wall is aligned with the cantilever axis and reaches a maximum when the domain wall is perpendicular to the cantilever axis. This indicates that the in-plane surface deformation is parallel to the domain wall. For this reason, only two sets of domain walls are seen in a single scan. This is clearly seen for two images of the same moiré pattern with the sample rotated by 90°, where domain walls perpendicular to the axis show high contrast and those parallel show weak contrast. However, recombining two images from orthogonal scans should be sufficient to reconstruct the original in-plane surface displacement, as depicted schematically in Fig. 3c. Figure 3g shows the reconstructed image derived from Fig. 3e and f, which closely agrees with the expected moiré pattern. From this analysis we can surmise that the applied out-of-plane electric field leads to an in-plane surface deformation that must be aligned along the length of the domain wall.

We next investigate the origin of the apparent electromechanical displacement oriented along the domain wall, focusing on the case of tBLG: since all the studied systems exhibit similar features in PFM originating from moiré patterns, our analysis can also be extended to them. We first note that in tBLG both AA ($P6/mmm$, point group $6/mmm$) and AB ($P\bar{3}m1$, point group $\bar{3}m$) stacking should not have a piezoelectric response. However, this symmetry is necessarily broken as the stacking changes from AB in the middle of the domains to AA and saddle point, which is always accompanied by formation of large strain gradients.

Generally, this symmetry-breaking can allow piezoelectric coupling to the out-of-plane field. This coupling of the piezoelectric response $e_{\alpha\beta\gamma}$ to the strain gradients $\frac{\partial\epsilon_{\lambda\mu}}{\partial x_\kappa}$ is described by a six-rank tensor $T_{\alpha\beta\gamma\kappa\lambda\mu}$:

$$e_{\alpha\beta\gamma} = T_{\alpha\beta\gamma\kappa\lambda\mu}\frac{\partial\epsilon_{\lambda\mu}}{\partial x_\kappa} \quad (1)$$

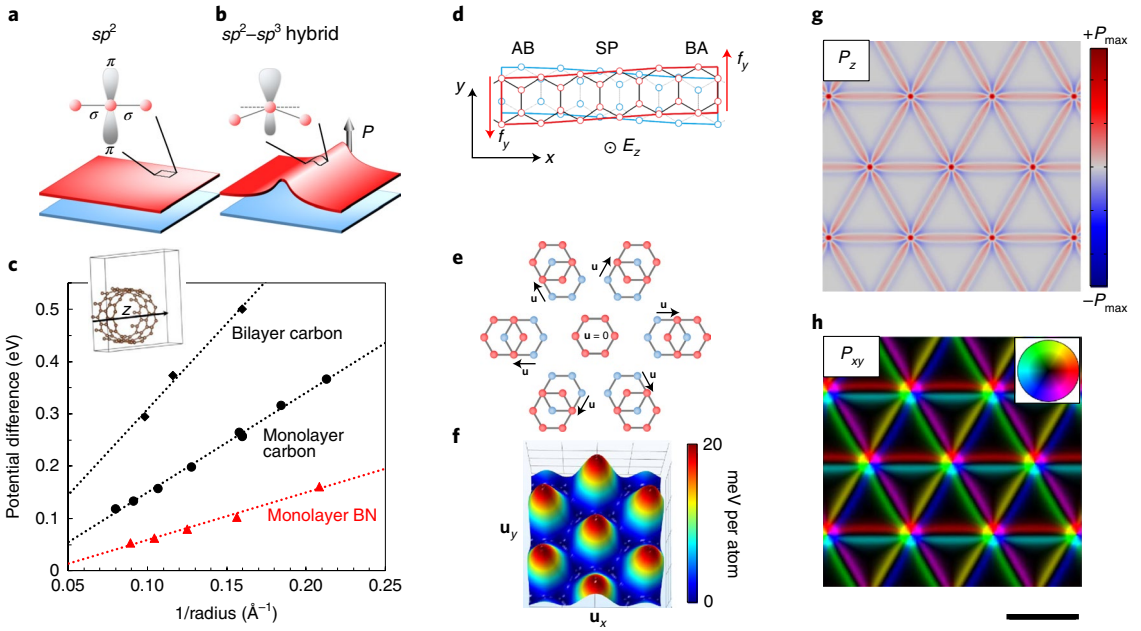

Fig. 4 | Strain-gradient and curvature induced polarization. a,**b**, In tBLG, a strain gradient leads to a bending of the σ-bonds from in-plane sp^2 (**a**) to a mixed in-plane/out-of-plane sp^2–sp^3 character (**b**) due to the curvature present at the domain walls; the asymmetric π orbitals give rise to an out-of-plane polarization, *P* (black arrow). **c**, Nanotubes of various materials and radii hence, strain, develop a potential difference from inside to outside of the nanotube along its radius (inset). **d**, A schematic of stacking order across a domain wall and the associated piezoelectric forces $\pm f_y$ due to an out-of-plane applied electric field E_z. **e**, The low-energy lateral shifts of a top graphene layer (red) relative to a lower layer (blue) gives AB-type stacking with sixfold symmetry and allows definition of the order parameter **u**. **f**, The Landau free energy landscape is shown with **u** = 0 at the local maxima. **g**,**h**, Calculation of flexoelectric coupling gives rise to out-of-plane polarization P_z localized at the highest strain-gradient regions; that is, AA sites and domain walls (**g**) while in-plane polarizations P_{xy} emerge in the vicinity of the domain walls with polar vectors of opposite direction and vortices surrounding the AA sites (**h**). Colour denotes direction of P_{xy} and strength gives magnitude. Scale bar in **h**, 50 nm.

where $e_{\alpha\beta\gamma}$ is defined as the stress $\sigma_{\beta\gamma}$ generated by applying electric field E_α:

$$\sigma_{\beta\gamma} = E_\alpha e_{\alpha\beta\gamma} \tag{2}$$

Strain gradients and their responses to electric fields can also be linked to polarization via the flexoelectric effect[22]. Here, a strain gradient gives rise to an electric polarization:

$$P_\alpha = \mu_{\alpha\beta\gamma\lambda}\frac{\partial \epsilon_{\gamma\lambda}}{\partial x_\beta} \tag{3}$$

This polarization then gives rise to a piezoelectric effect under the influence of an electric field. An alternative to the flexoelectric effect is a direct coupling of strain gradients to piezoelectric stresses, without the necessity for the existence of a polarization in the material. We will quantify the magnitude of both of these effects for twisted bilayer graphene next, and then make general remarks about other materials.

We start with the flexoelectric effect. For graphene and bilayer graphene at small displacement field, the large in-plane conductivity will screen lateral polarizations, so we only need to consider out-of-plane polarizations generated via the flexoelectric effect; that is, the coefficients $\mu_{zz,xx}$, and $\mu_{zx,zx}$ (see Supplementary Fig. 4 for schematics). Figure 4a,b gives a physical view of the origin of this polarization; flat graphene sheets have planar σ bonds and symmetric π bonds out of the plane. However, when a curvature is present the bonds bend away from purely planar in character to possess a component of sp^3 bonding (Fig. 4b) as opposed to the purely sp^2 case of flat graphene (Fig. 4a). This causes an asymmetric distribution of the electron orbitals and hence gives rise to a polarization[23–26]. It is challenging to directly model the polarization at a domain wall in twisted bilayer graphene; instead, to estimate the magnitude of these coefficients, we perform calculations on carbon nanotubes (Fig. 4c). As demonstrated in refs. [23,24], the curvature of the nanotube induces a polarization, which scales linearly with the inverse radius of the nanotube; that is, the gradient of strain. This is manifested as a potential change over the nanotube, which is calculated (see Methods) along the radial line shown in the inset to Fig. 4c. To make a closer connection to bilayer graphene, we also plot potential differences for double-walled nanotubes in Fig. 4c and find that additional layers are approximately additive in terms of the voltage drop. For our purposes, the slope of the lines in Fig. 4c can be converted into an estimate for the shear flexoelectric coefficient $\mu_{zx,zx}$ (see Supplementary Information Section 4 for details); for bilayer graphene we obtain $\mu_{zx,zx} \simeq -0.03\,\mathrm{nC\,m^{-1}}$. This is of the same order as the shear clamped-ion flexoelectric coefficients; for example, in perovskite oxides[27,28]. Therefore, if we assume 70 pm buckling of the monolayer over 10 nm (ref. [10]) we obtain $P_z = 0.002\,\mu\mathrm{C\,cm^{-2}}$. This result is low compared to typical values found in ferroelectric materials where polarization is usually tens of microcoulombs per centimetre squared; for example, in $BaTiO_3$, $P_z = 25\,\mu\mathrm{C\,cm^{-2}}$. However, the exact value is likely to strongly depend on the local strain gradient that may not be uniform across the domain wall or AA site.

We next consider the direct coupling of strain gradients to piezoelectric stresses. In Supplementary Information Section 5 we list the symmetry-allowed piezoelectric responses as a result of this coupling. In particular, we consider the components:

$$e_{zyz} = C_1\frac{\partial \epsilon_{xy}}{\partial x}, \tag{4}$$

$$e_{zxy} = C_2\frac{\partial \epsilon_{xy}}{\partial z} \tag{5}$$

where x is the direction normal to the wall and C_1 and C_2 are material-dependent constants. The first expression here describes the shear piezoelectric coefficient e_{zyz} in relation to the shear gradient $\frac{\partial \epsilon_{xy}}{\partial x}$, closely tied to the flexoelectric effect described by coefficient $\mu_{zx,zx}$. In contrast, the second term presents an entirely new coupling, given by the difference of the shear strain at top and bottom layers; in effect, a direct strain-gradient-induced piezoelectricity that leads to the observed PFM contrast without induction of polarization. To estimate the magnitude of these effects, we conducted density functional theory (DFT) calculations of a simplified model of a domain wall similar to those in tBLG (that is, where the stacking goes from AB → SP → BA → SP). We start by setting an out-of-plane corrugation of the top graphene layer, modelling the situation described in Supplementary Information Section 4 and apply an out-of-plane electric field to the system. We then introduce in-plane shear strains and strain gradients (details in Supplementary Information Section 5). In the latter case, application of the out-of-plane electric field leads to appearance of forces acting on the top layer along the wall along with elastic stresses that are roughly proportional to $\frac{\partial \epsilon_{xy}}{\partial x} E_z$, (Fig. 4d) agreeing with our symmetry considerations. Analysing the results of our DFT simulations, we can estimate (see Supplementary Information Section 5 for details) that a measurable surface displacement of the domain wall of 0.1–1 pm is expected at applied electric fields of 10–100 MV cm^{-1}, which, while high, is not unreasonable since electric fields may reach large values near the tip apex. We have therefore shown a fundamental possibility of surface displacement along the wall induced by an out-of-plane electric field in free-standing bilayer graphene (Fig. 4d). In reality, other mechanisms can contribute to the piezoelectric response, such as substrate interactions or bandgap opening, but that is beyond the scope of this section.

Both of the mechanisms described here in general contribute to the observed PFM contrast in the various materials studied. In the case of semiconducting or insulating systems, in-plane polarizations can also be sustained that can give rise to larger in-plane piezoelectric response. For a generic insulating material, we conducted finite-element simulations of the polarization developed for various stacking configurations between the two layers of a bilayer. A given stacking configuration is defined by the relative lateral translation of the two layers $\mathbf{u}$ with $\mathbf{u} = 0$ corresponding to AA stacking (see Fig. 4e for schematic stackings). The energetic landscape as a function of order parameter is displayed in Fig. 4f (see Methods for details). For each of these configurations, we calculate the out-of-plane (Fig. 4g) and in-plane (Fig. 4h) polarizations, respectively. The out-of-plane polarization is maximized at the AA site with smaller responses along the domain wall, while the in-plane response shows polar vorticity at the AA sites and strong response along the domain walls.

Strain gradients are an inherent part of moiré superlattices and here we have shown that in the regions where these are to be found there are previously undiscovered physical phenomena. In particular, the existence of polarizations in moiré structures has consequences for both the electronic and optical properties of these materials. Electronically, the presence of a polarization implies a strong modification of wavefunction extent within a moiré site, the dielectric screening properties and consequently the magnitude of Coulomb interactions. Optically, the presence of dipole moments in the moiré structures will modify the optical response both qualitatively (via selection rules) and quantitatively (via the dielectric properties of the system). A complete low-energy theoretical analysis of these issues and exploration of their consequences for the optoelectronics properties remains an open problem.

Online content

Any methods, additional references, Nature Research reporting summaries, source data, extended data, supplementary information, acknowledgements, peer review information; details of author contributions and competing interests; and statements of data and code availability are available at https://doi.org/10.1038/s41565-020-0708-3.

Received: 4 February 2020; Accepted: 5 May 2020;
Published online: 22 June 2020

References

1. Cao, Y. et al. Unconventional superconductivity in magic-angle graphene superlattices. *Nature* **556**, 43–50 (2018).
2. Yankowitz, M. et al. Tuning superconductivity in twisted bilayer graphene. *Science* **363**, 1059–1064 (2019).
3. Sharpe, A. L. et al. Emergent ferromagnetism near three-quarters filling in twisted bilayer graphene. *Science* **365**, 605–608 (2019).
4. Huang, S. et al. Topologically protected helical states in minimally twisted bilayer graphene. *Phys. Rev. Lett.* **121**, 037702 (2018).
5. Sunku, S. S. et al. Photonic crystals for nano-light in moiré graphene superlattices. *Science* **362**, 1153–1156 (2018).
6. Seyler, K. L. et al. Signatures of moiré-trapped valley excitons in $MoSe_2/WSe_2$ heterobilayers. *Nature* **567**, 66–70 (2019).
7. Cao, Y. et al. Correlated insulator behaviour at half-filling in magic-angle graphene superlattices. *Nature* **556**, 80–84 (2018).
8. Yoo, H. et al. Atomic and electronic reconstruction at the van der Waals interface in twisted bilayer graphene. *Nat. Mater.* **18**, 448–453 (2019).
9. Alden, J. S. et al. Strain solitons and topological defects in bilayer graphene. *Proc. Natl Acad. Sci. USA* **110**, 11256–11260 (2013).
10. Zhang, C. et al. Interlayer couplings, moiré patterns, and 2D electronic superlattices in MoS_2/WSe_2 hetero-bilayers. *Sci. Adv.* **3**, e1601459 (2017).
11. Kerelsky, A. et al. Maximized electron interactions at the magic angle in twisted bilayer graphene. *Nature* **572**, 95–100 (2019).
12. Gargiulo, F. & Yazyev, O. V. Structural and electronic transformation in low-angle twisted bilayer graphene. *2D Mater.* **5**, 015019 (2017).
13. Chandratre, S. & Sharma, P. Coaxing graphene to be piezoelectric. *Appl. Phys. Lett.* **100**, 023114 (2012).
14. Ong, M. T. & Reed, E. J. Engineered piezoelectricity in graphene. *ACS Nano* **6**, 1387–1394 (2012).
15. da Cunha Rodrigues, G. et al. Strong piezoelectricity in single-layer graphene deposited on SiO_2 grating substrates. *Nat. Commun.* **6**, 7572 (2015).
16. Wang, X. et al. Observation of a giant two-dimensional band-piezoelectric effect on biaxial-strained graphene. *NPG Asia Mater.* **7**, e154–e154 (2015).
17. Van der Donck, M., De Beule, C., Partoens, B., Peeters, F. M. & Van Duppen, B. Piezoelectricity in asymmetrically strained bilayer graphene. *2D Mater.* **3**, 035015 (2016).
18. Balke, N. et al. Differentiating ferroelectric and nonferroelectric electromechanical effects with scanning probe microscopy. *ACS Nano* **9**, 6484–6492 (2015).
19. Kalinin, S. V., Jesse, S., Tselev, A., Baddorf, A. P. & Balke, N. The role of electrochemical phenomena in scanning probe microscopy of ferroelectric thin films. *ACS Nano* **5**, 5683–5691 (2011).
20. Labuda, A. & Proksch, R. Quantitative measurements of electromechanical response with a combined optical beam and interferometric atomic force microscope. *Appl. Phys. Lett.* **106**, 1–5 (2015).
21. Kalinin, S. V. et al. Vector piezoresponse force microscopy. *Microsc. Microanal.* **12**, 206–220 (2006).
22. Wang, B., Gu, Y., Zhang, S. & Chen, L.-Q. Flexoelectricity in solids: progress, challenges, and perspectives. *Prog. Mater. Sci.* **106**, 100570 (2019).
23. Dumitrică, T., Landis, C. M. & Yakobson, B. I. Curvature-induced polarization in carbon nanoshells. *Chem. Phys. Lett.* **360**, 182–188 (2002).
24. Kalinin, S. V. & Meunier, V. Electronic flexoelectricity in low-dimensional systems. *Phys. Rev. B* **77**, 033403 (2008).
25. Kothari, M., Cha, M. & Kim, K. Critical curvature localization in graphene. I. Quantum-flexoelectricity effect. *Proc. R. Soc. A* **474**, 20180054 (2018).
26. Kundalwal, S. I., Meguid, S. A. & Weng, G. J. Strain gradient polarization in graphene. *Carbon* **117**, 462–472 (2017).
27. Dreyer, C. E., Stengel, M. & Vanderbilt, D. Current-density implementation for calculating flexoelectric coefficients. *Phys. Rev. B* **98**, 075153 (2018).
28. Stengel, M. Surface control of flexoelectricity. *Phys. Rev. B* **90**, 201112 (2014).

Methods

Sample fabrication. Samples were prepared using the standard polymer stamp dry-transfer technique on a modified optical microscope with heating stage and rotation stage. A glass slide with a polydimethylsiloxane stamp coated in a thin polypropylene carbonate film is brought into contact with individual flakes previously exfoliated onto SiO_2/Si via standard methods. In this way a thick BN flake is first picked up and then placed in contact with approximately half of a large graphene monolayer. During pick-up the graphene monolayer tears along the edge of the BN. The desired twisted angle is then made through rotational misalignment of the picked-up partial graphene monolayer and the remaining portion of the graphene on SiO_2/Si. After the second graphene pick-up the polypropylene carbonate is carefully removed from the polydimethylsiloxane stamp and placed onto a SiO_2/Si chip (heated for better adhesion). Other material samples for example WSe_2 are fabricated in a similar manner.

PFM. In PFM an AC bias is applied between the tip and sample that induces a periodic deformation of the sample whose amplitude and phase give local information on the electromechanical response. Experiments were performed on a Bruker Dimension Icon with a Nanoscope V Controller. Typically, Oxford Instrument Asylum Research ASYELEC-01 Ti/Ir coated silicon probes a force constant of ~3 N m^{-1} were used. The radius of curvature is 25 nm. However, the relevant quantify for PFM resolution is the 'contact radius', which, for the low loading forces of less than the roughly 50 nN routinely used in this work, would generally be ~5 nm. This produced the best imaging while also maintaining good tip apex quality. Generally, AC bias magnitudes were <1 V with resonance frequencies in the range of ~300 kHz for vertical and 750–850 kHz for lateral PFM. Single frequency excitation at the resonance peak was found to give stable imaging conditions as the peaks did not shift appreciably (that is, <500 Hz) as surface roughness on such atomically flat surfaces is minimal. An example resonance peak is given in Supplementary Fig. 6. Amplitude values are displayed in arbitrary units as calibration is challenging and unreliable for comparison between different cantilevers. Results were confirmed on an Oxford Instruments Asylum Research Cypher atomic force microscope operating in the dual-AC resonance tracking mode (Supplementary Fig. 7).

DFT. DFT calculations of nanotubes are performed using the Perdew, Burke and Ernzerhof generalized gradient functional[29] and projector-augmented wave[30] implemented in the VASP package[31]. A Monkhorst–Pack[32] k mesh of $10\times1\times1$ (with ten points in the direction parallel to the nanotube) and an energy cutoff for the plane-wave basis set of 500 eV was used. No atoms were allowed to relax in the calculations; the C–C (B–N) distance was fixed to 1.42 (1.45) Å.

Calculations of the tBLG piezoelectric response are done in the framework of the local density approximation to DFT with the in-house code LAUTREC. Atomic cores are represented by normal-conserving pseudopotentials in the Troullier–Martins form. The bilayer structures are built by placing two graphene sheets at a fixed distance of 6.3 bohr, close to the calculated equilibrium distance within local density approximation. The out-of-plane cell parameter is set to 30 atomic units (a.u.), which provides enough vacuum to decouple the system from its periodically repeated images. Each sheet is distorted by a sinusoidal acoustic wave, where the amplitude in the two layers has opposite signs. The amplitude is set in such a way that maxima and minima correspond to AB or BA stacking, respectively. No further relaxation is considered. The Brillouin zone of the 16-cell geometry is sampled by a $1\times4\times36$ Monkhorst–Pack grid of k points (for smaller/larger geometries we used equivalent or denser grids). We use a plane-wave cutoff of 80 Ry. The out-of-plane electric field is applied by introducing a suitable external dipole layer within the vacuum region.

Finite-element simulations. The following energy functional W was used for finite-element calculations:

$$\begin{aligned} W &= V(\mathbf{u}) + W_{\text{elast}},\\ W_{\text{elast}} &= \tfrac{C_{11}}{2}\left(\epsilon_{11}^2+\epsilon_{22}^2\right) + C_{12}\epsilon_{11}\epsilon_{22} + (C_{11}-C_{12})\epsilon_{12},\\ \epsilon_{11} &= \tfrac{\partial u_1}{\partial x}, \epsilon_{22} = \tfrac{\partial u_2}{\partial y}, \epsilon_{12} = \tfrac{1}{2}\left(\tfrac{\partial u_1}{\partial y}+\tfrac{\partial u_2}{\partial x}\right),\\ C_{11} &= \tfrac{E^{2D}}{1-\nu^2}, C_{12} = \tfrac{\nu E^{2D}}{1-\nu^2}, \end{aligned}$$

where $V(\mathbf{u})$ is the sixfold-symmetric periodic potential due to van der Waals (vdW) interlayer interaction shown in Fig. 4f (refs.[9,33]), W_{elast} is the elastic energy of the top layer and ϵ_{ij} is the two-dimensional elastic strain of the top layer. For our simulations, we use Young modulus $E^{2D} = 340$ N m^{-1} and Poisson ratio $\nu = 0.3$ (ref. [9]).

In our simulations, we set the initial distribution of the order parameter $(u_1, u_2) = (\theta y, -\theta x)$, corresponding to the rotation of the top graphene layer by a small angle θ, and let the system relax until the minimal energy is reached. As a result, the domain structure is reached with a_0/θ, with clearly defined domain walls and vortices.

Data availability

Data is available from the corresponding author upon request.

References

29. Perdew, J. P., Burke, K. & Ernzerhof, M. Generalized gradient approximation made simple. *Phys. Rev. Lett.* **77**, 3865 (1996).
30. Blöchl, P. E. Projector augmented-wave method. *Phys. Rev. B* **50**, 17953 (1994).
31. Kresse, G. & Furthmüller, J. Efficient iterative schemes for ab initio total-energy calculations using a plane-wave basis set. *Phys. Rev. B* **54**, 11169 (1996).
32. Monkhorst, H. J. & Pack, J. D. Special points for brillouin-zone integrations. *Phys. Rev. B* **13**, 5188 (1976).
33. Popov, A. M., Lebedeva, I. V., Knizhnik, A. A., Lozovik, Y. E. & Potapkin, B. V. Commensurate-incommensurate phase transition in bilayer graphene. *Phys. Rev. B.* **84**, 045404 (2011).

Acknowledgements

This work is supported by the Programmable Quantum Materials (Pro-QM) programme at Columbia University, an Energy Frontier Research Center established by the Department of Energy (grant no. DE-SC0019443). L.J.M. acknowledges support from the Swiss National Science Foundation (grant no. P400P2_186744). Synthesis of $MoSe_2$ and WSe_2 was supported by the National Science Foundation Materials Research Science and Engineering Centers programme through Columbia in the Center for Precision Assembly of Superstratic and Superatomic Solids (DMR-1420634). The Flatiron Institute is a division of the Simons Foundation. C.E.D. acknowledges support from the National Science Foundation under grant no. DMR-1918455. M.S. and K.S. acknowledge the support of the European Research Council under the European Union's Horizon 2020 research and innovation programme (grant agreement no. 724529), Ministerio de Economia, Industria y Competitividad through grant nos. MAT2016-77100-C2-2-P and SEV-2015-0496, and the Generalitat de Catalunya (grant no. 2017SGR 1506). We thank D. Griffin and T. Walsh from Oxford Instruments Asylum Research for confirmation of PFM results.

Author contributions

L.J.M. conceived the concept of the study and initiated the first PFM experiments. A.K., N.R.F., E.-M.S., A.G., Y.Z., S.L.M., W.W., Y.B. and L.Z. provided additional samples and experimental results. K.S., M.S. and C.E.D performed theoretical calculations and simulations. K.W. and T.T. provided hBN crystals. J.H., X.Z., D.N.B., C.D., C.E.D. and A.N.P. advised. L.J.M and A.N.P. wrote the manuscript with assistance from all authors.

Competing interests

The authors declare no competing interests.

Additional information

Extended data is available for this paper at https://doi.org/10.1038/s41565-020-0708-3.

Supplementary information is available for this paper at https://doi.org/10.1038/s41565-020-0708-3.

Correspondence and requests for materials should be addressed to A.N.P.

Reprints and permissions information is available at www.nature.com/reprints.

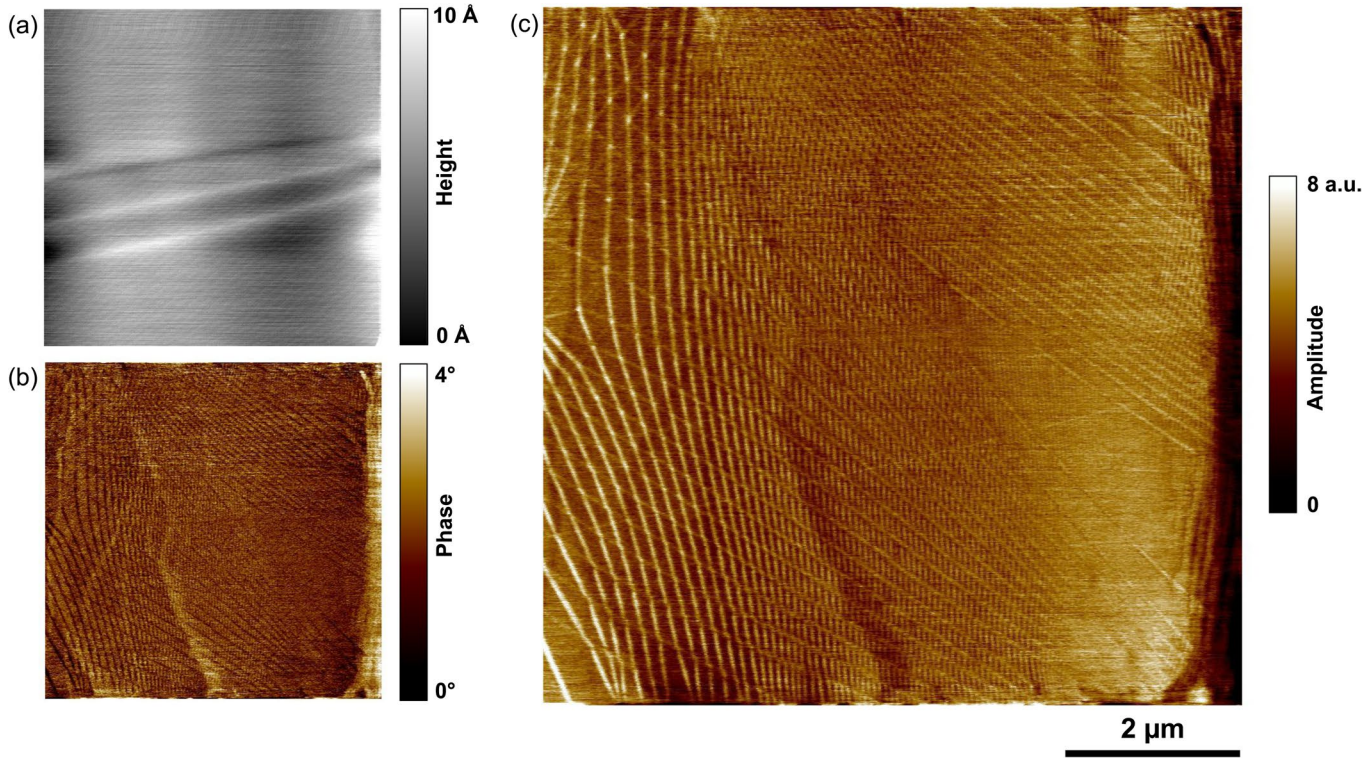

Extended Data Fig. 1 | Example of large-scale mapping of moiré superlattice. A lateral PFM image for a scan of $8 \times 8\,\mu m^2$; topography (**a**), phase (**b**) and amplitude (**c**) demonstrating that this technique can be used to observe the moiré across length scales that span orders of magnitude. Note the huge variation in moiré wavelength from ~500 to ~50 nm and presence of large strains.

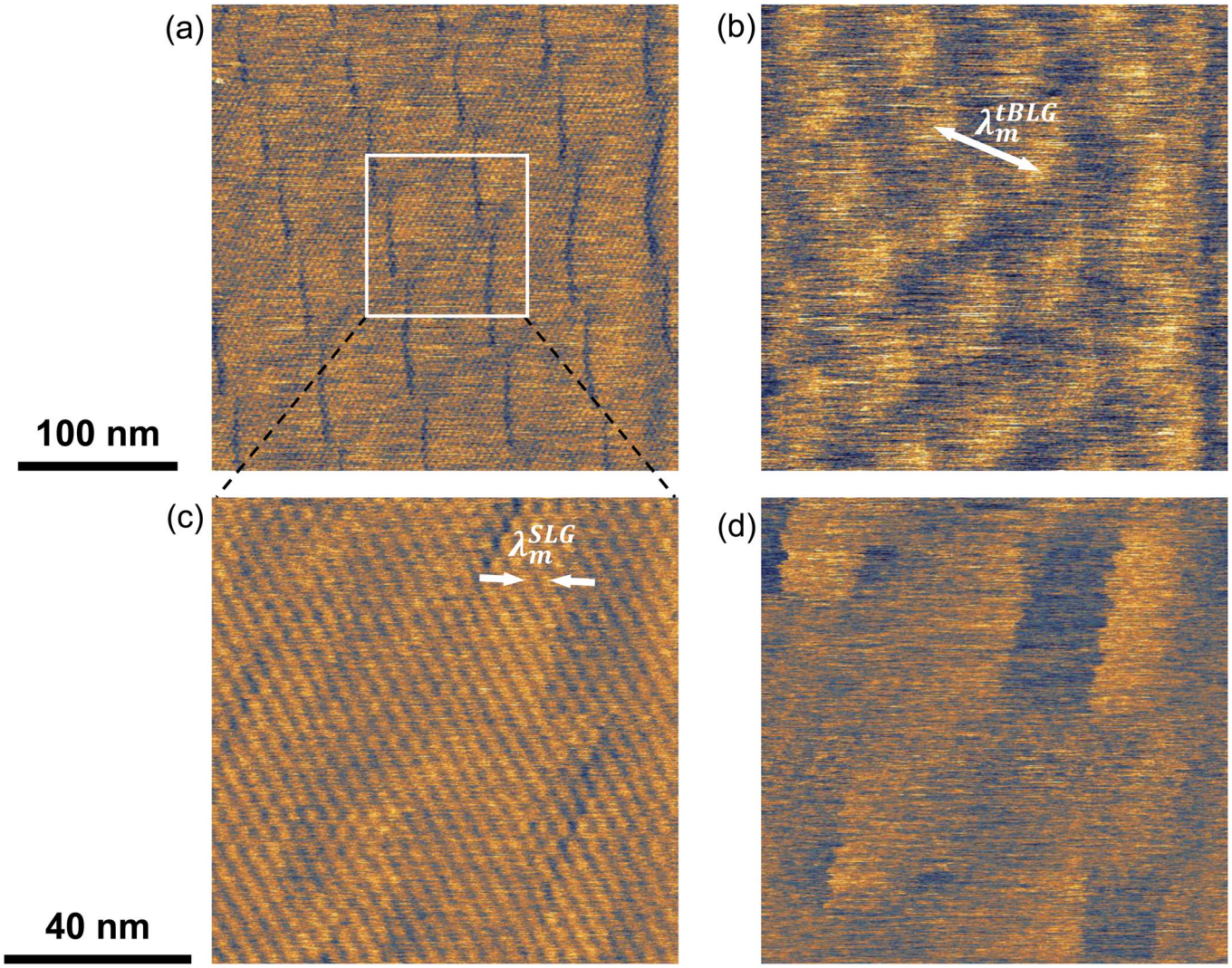

Extended Data Fig. 2 | Example of mapping of two co-existing moiré superlattices. Amplitude (**a**) and phase (**b**) images clearly show a strained moiré superlattice due to the twisted bilayer of graphene with wavelength $\lambda_m^{tBLG} \sim 70$ nm and a second smaller wavelength related to the bottom layer of graphene with the hBN flake of $\lambda_m^{SLG} \sim 4.5$ nm.